

MICROSCOPY

Direct optical measurement of intramolecular distances with angstrom precision

Steffen J. Sahl^{1*}, Jessica Matthias^{2,†}, Kaushik Inamdar^{1,3,‡}, Michael Weber^{1,‡}, Taukeer A. Khan¹, Christian Brüser^{1,4}, Stefan Jakobs^{1,3,4,5}, Stefan Becker⁶, Christian Griesinger^{5,6}, Johannes Broichhagen^{7,§}, Stefan W. Hell^{1,2,5*}

Optical investigations of nanometer distances between proteins, their subunits, or other biomolecules have been the exclusive prerogative of Förster resonance energy transfer (FRET) microscopy for decades. In this work, we show that MINFLUX fluorescence nanoscopy measures intramolecular distances down to 1 nanometer—and in planar projections down to 1 angstrom—directly, linearly, and with angstrom precision. Our method was validated by quantifying well-characterized 1- to 10-nanometer distances in polypeptides and proteins. Moreover, we visualized the orientations of immunoglobulin subunits, applied the method in human cells, and revealed specific configurations of a histidine kinase PAS domain dimer. Our results open the door for examining proximities and interactions by direct position measurements at the intramolecular scale.

Owing to its minimal invasiveness, fluorescence microscopy has played a central role in the quest for understanding the myriad of functions of biomolecules. However, this endeavor calls for the quantification of sizes, associations, and conformational changes of proteins and other biomolecules, which in turn requires precise measurements of inter- and intramolecular distances, r , equal to 1 to 20 nm. Although measuring such distances is clearly challenged by diffraction, subdiffraction (super)resolution fluorescence microscopy also struggles with this task. Indeed, since the 1960s, macromolecular distances have been inferred indirectly, namely by the phenomenon called Förster resonance energy transfer (FRET) (1). FRET deduces distances r from the probability with which an excited fluorophore transfers its excited state energy to an electronically relaxed fluorophore that features a longer excitation and emission wavelength and is located further away by r . As the only optical method to explore proximities <10 nm in both protein ensembles and on the individual protein level, FRET (2–4) has become one

of the most popular methods in the life sciences. Dubbed a “molecular ruler,” FRET has thus led to many insights both in cells and in vitro studies of biomolecules (5–7).

FRET, however, entails experimental provisions stemming from the indirect nature of the measurement (5). Because the energy transfer occurs through an interaction of the two transition dipole moments of the fluorophores, the result varies inversely with the sixth power of the distance, $1/r^6$, rendering FRET a highly nonlinear ruler (6, 7). Moreover, although reproducible results for distance measurements have been demonstrated with a range of carefully established correction factors (8, 9), the FRET process fundamentally depends on the usually uncontrolled relative orientation of the two transition dipoles and on the polarizability of the molecules between them. This altogether makes reliable determinations of r without prior knowledge about the molecular details of the system challenging and occasionally impossible. The situation is exacerbated by the fact that FRET measurements are, in practice, limited to (at most) 2 to 8 nm, because outside this range the dipole-dipole interaction hardly modulates with r . All these factors can lead to considerable uncertainties, making FRET much better at providing “yes” or “no” answers regarding colocalization in cells or large molecular ensembles than at determining exact (intra)molecular distances.

In principle, nanometer-scale proximities between two spectrally shifted fluorophores with different excitation and/or emission wavelengths can be measured (10–12) because the spectral shift allows for the separation of the fluorophores despite diffraction. Provided the spectral shift is sufficient, each fluorophore can be localized by calculating the centroid of its fluorescence diffraction spot rendered on a camera. Ironically, in the sought-after range of $r \leq 8$ nm, the spectral shift undesirably elicits

FRET between the fluorophores, thus hampering their independent emission. Independence can be gained by ensuring that the fluorophores emit sequentially, through an on-off switching of their fluorescence, as in the super-resolution (13) method called photoactivated localization microscopy (PALM) or stochastic optical reconstruction microscopy (STORM) (14–16). However, reversible on-off switching does not decouple the fluorophores entirely, and for distances <10 nm, this residual coupling (17) elevates bleaching (18).

Improved emission independence can be gained by binding fluorophores transiently to the sites of interest, as in the method called points accumulation for imaging in nanoscale topography (PAINT) (19), which is highly effective when mediated by DNA hybridization (20, 21). Although subnanometer localization precisions can be obtained (22), DNA-PAINT requires that the sites of interest be decorated with and accessed by labeled single strands of DNA. This labeling procedure is, by far, more restricting than directly attaching a fluorophore at the protein site of interest because not all biomolecules can be labeled by DNA oligonucleotides. Moreover, the oligonucleotides do not pass the living cell membrane, and the fluorophore labels need constant replenishment by fresh labels from the surrounding solution. Finally, the highly charged DNA may affect the molecular conformation (23).

Conceptually even more serious at molecular distances are the fundamental limitations of localizing a fluorophore by establishing the centroid of its fluorescence diffraction spot on a camera. First, centroid calculation critically relies on the detection of many fluorescence photons because the localization precision σ scales with $1/\sqrt{N}$, with N being the total number of detected photons in the camera spot. Thus, the need to wait for many emissions entails frequent excursions of the fluorophore to transient, nonemitting states, sample drift, and bleaching. Second, unless the fluorophore emits isotropically in space, which is virtually impossible given that it is target-bound, the dipole nature of emission leads to systematic deviations of the centroid position from the actual position of the molecule (24–27), which can frequently exceed 10 nm. Because the rotational freedom and the emission (an)isotropy are a priori unknown, these deviations mandate special caution regarding the accuracy of any method based on centroid determination.

In this work, we show that MINFLUX localization (28) determines (intra)molecular distances linearly and with subnanometer precision at room temperature. In MINFLUX localization, the fluorophore position is established by relating, and ideally matching, the known position of a central zero of a doughnut-shaped excitation beam to the unknown position of the fluorophore (Fig. 1A). Thus, MINFLUX implies

¹Department of NanoBiophotonics, Max Planck Institute for Multidisciplinary Sciences, Göttingen 37077, Germany.

²Department of Optical Nanoscopy, Max Planck Institute for Medical Research, Heidelberg 69120, Germany. ³Department of Neurology, University Medical Center Göttingen, Göttingen 37075, Germany. ⁴Fraunhofer Institute for Translational Medicine and Pharmacology ITMP, Translational Neuroinflammation and Automated Microscopy TNM, Göttingen 37075, Germany.

⁵Cluster of Excellence “Multiscale Bioimaging: from Molecular Machines to Networks of Excitable Cells” (MBExC), University of Göttingen, Göttingen, Germany. ⁶Department of NMR-based Structural Biology, Max Planck Institute for Multidisciplinary Sciences, Göttingen 37077, Germany. ⁷Department of Chemical Biology, Max Planck Institute for Medical Research, Heidelberg 69120, Germany.

*Corresponding author. Email: steffen.sahl@mpinat.mpg.de (S.J.S.); stefan.hell@mpinat.mpg.de (S.W.H.)

[†]Present address: Abberior Instruments America, Bethesda, MD 20814, USA.

[‡]These authors contributed equally to this work.

[§]Present address: Leibniz-Forschungsinstitut für Molekulare Pharmakologie, Berlin 13125, Germany.

a minimization rather than a maximization of the number of required fluorescence photons. Because in MINFLUX localization the localization precision σ scales exponentially with the number of detected photons e^{-N} , the issues of camera-based localization are overcome. Indeed, MINFLUX typically requires about 100 times fewer detected photons to reach the camera localization precision (28, 29). By using photoactivatable (caged) fluorophores, emission orthogonality can also be ensured such that one fluorophore emits while the other one remains fully inert to the excitation. Additionally, the localization of the fluorophores with a circularly polarized doughnut zero renders the localization largely independent of their orientation. The resulting reliable determination of each fluorophore's coordinates has enabled us to measure static molecular distances directly, that is, without mediation by a multifactorial process such as FRET. Quantifying 1- to 20-nm distances has thus

allowed us to visualize, for example, the end-to-end distance of a small 16-kDa protein or provide access to conformational details of a larger 150-kDa protein by direct positional measurements of the reporter fluorophores.

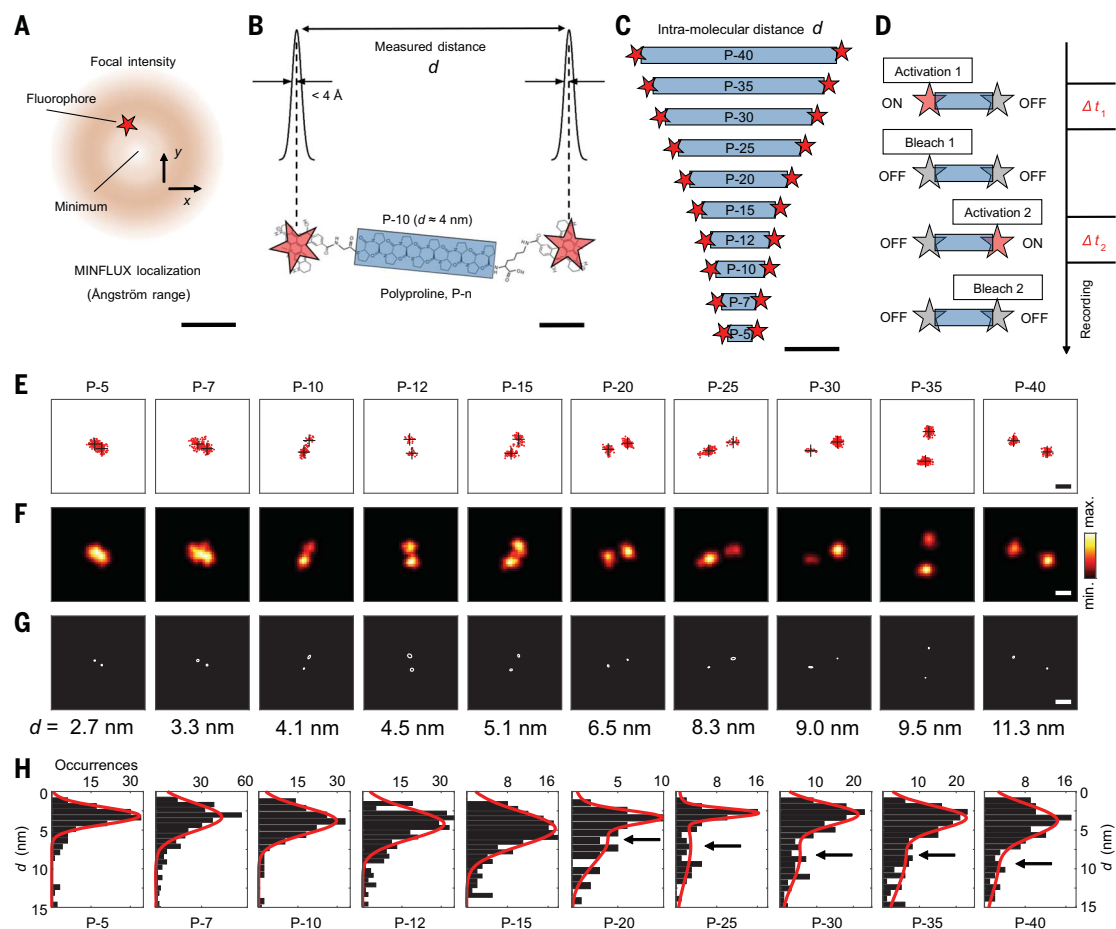
MINFLUX as a linear ruler in the <10-nm (intra)molecular range

To explore the potential of the chosen MINFLUX protocol (Fig. 1A and methods), we initially turned to the polyproline helix secondary structure as a distance reference. The widely assumed rigidity of this polypeptide (30, 31), especially for low to intermediate numbers (<20) of repeats, allows the positioning of fluorophores at defined distances. Indeed, polyprolines enabled Stryer and Haugland to demonstrate (32) the $1/r^6$ FRET dependence in the 1960s, which was put forward by Förster in 1948. Polyprolines also allowed Schuler, Eaton, and co-workers to demonstrate distance-dependent FRET at the single-molecule level (33).

Conjugation of the photoactivatable dye DiMeO-ONB-SiR637 (34) to both ends of polyproline chains P- n , where n is the number of proline residues (P), with N- and C-terminal glycine or lysine residues produced putatively linear unimolecular systems (Fig. 1B). The synthesis was controlled to yield peptides without variation in the proline repeat number, meaning that the interfluorophore distance d was tunable from <3 nm (for P-5) to >10 nm (for P-40), taking as an expectation the highly extended type II (PPII) helix lengths with all-trans peptide bonds (Fig. 1C). The peptides were nonspecifically immobilized on the surface of a poly-L-lysine coated cover glass at high dilution and examined individually (see materials and methods).

To quantify the localization precision for individual fluorophores at the end of the polyprolines, we initially imaged samples of a separated fraction of mono-labeled P-15 polyproline. Fluorophores that exhibited noticeable positional

Fig. 1. Angstrom-precise intramolecular distance measurements based on direct optical measurements of positions in and beyond the FRET range. (A) MINFLUX approaches a fluorophore (red star, not to scale) with an illumination intensity minimum (center of doughnut pattern) to achieve its precise localization. **(B)** Tunable distances provided by polyproline, a peptide composed of relatively rigid helices of defined repeat number, terminal glycine and lysine residues, and identical photoactivatable fluorophores conjugated to both ends. The angstrom-range MINFLUX localization precision enables measurements of 1- to 10-nm intramolecular distances. **(C)** Prepared polyproline constructs: P- n , with $n = 5, 7, 10, 12, 15, 20, 25, 30, 35$, or 40, constituting a distance ladder. Expected end-to-end distances, assuming a type II helix in molecular dynamics simulations, range from ~2.5 to ~11 nm (33). **(D)** Sequential photoactivation used for addressing the fluorophores individually and in molecular proximity. **(E to G)** MINFLUX reconstructions of polyproline end-to-end distances, displayed as (E) localization sets (red points) and the localized dye coordinates (black crosses), (F) 2D histogram representation, and (G) inferred dye positions and their respective measurement precision. The ellipses correspond to 3σ contours. The extracted distance d is indicated below each example. **(H)** Distributions of measured distances d from P-5 to P-40. For 20 or more residues, long distances can be discerned in a broad second peak (indicated by arrows), but most end-to-end distances observed on the surface were found to be shorter (first peak). Red curves are Gaussian fits. Scale bars are 200 nm (A), 1 nm (B), 3 nm (C), and 5 nm [(E) to (G)].



fluorophores that exhibited noticeable positional

drifts owing to insufficient immobilization were excluded from analysis. Photoactivation was ensured by a regularly focused 405-nm beam that was co-aligned with the 640-nm doughnut-shaped excitation beam. After activation of DiMeO-ONB-SiR637 by cleavage of the *ortho*-nitrobenzyl carbamates, the fluorophore was transferred from an inactive off state to an active on state with photostable red emission. Once an active fluorophore was identified, the MINFLUX localization algorithm ensured that the excitation doughnut rapidly zoomed in on the emitter (35, 36). The final two MINFLUX iterations (36) were repeated until photobleaching, which rendered extended sets of successive fluorophore position estimates (fig. S1). From these raw localization data, the statistical localization precision could be inferred directly. For example, for only 150 photons in the final MINFLUX iteration, we obtained $\sigma_{\text{raw}} = 2.2 \pm 0.2$ nm. Aggregation of groups of 5 and 10 consecutive localizations yielded datasets with a smaller spatial spread, namely $\sigma_{5 \text{ combined}} = 1.2 \pm 0.2$ nm and $\sigma_{10 \text{ combined}} = 0.9 \pm 0.2$ nm, respectively.

The mean position of the fluorophore, that is, its time-averaged center of mass, is subject to an even lower uncertainty owing to the combined information from even more equivalent position determinations obtained for long on times. In practice, the localization precision was estimated to be on the order of the microscope's active-feedback stabilization per measurement time interval (0.1 to 0.3 nm) for the >1000 localizations obtained on average. Under the assumption of stationary fluorophore centers, the mean of all localizations can be assigned with (sub)angstrom precision depending on the numbers of localizations accrued (fig. S1). Note that the stabilized MINFLUX system (36), including beamline monitoring, did not require further processing of localization data to correct for drifts.

Moving to polyprolines with two DiMeO-ONB-SiR637 dyes, we observed that, apart from a fraction of already activated fluorophores at the beginning of the measurement, the emitters were indeed activated and localized independently (Fig. 1D). Localization of a fluorophore was terminated by a photobleaching event. Because the activation probability, controlled by the 405-nm laser power, was kept low, the activation of the second fluorophore frequently occurred seconds to minutes later (fig. S2), showing that the activation of the two fluorophores was indeed independent.

Precise and accurate distance measurements in the FRET range

MINFLUX allowed for quantification of the fluorophore-fluorophore distance (Fig. 1, E to G, and fig. S3) from P-40, with examples in the range $d \approx 10$ to 12 nm, over intermediate spacings (e.g., P-30; $d \approx 8$ to 9 nm) down to

spacings deep within the FRET range (e.g., P-15; $d \approx 5$ nm); the shortest tested peptide was P-5 ($d \leq 3$ nm). The subnanometer precision of individual position measurements produced data that were easy to evaluate even at small values of d .

The distributions of measured distances (Fig. 1H) were generally broad, and especially so for the longer polyprolines. This broadening, interpreted to result from a considerable flexibility in the peptide chain, had also been observed in the single-molecule FRET data and was described in simulations (33). For oligomers with $n \geq 20$, we observed rather broad peaks in the respective ranges that were expected for largely extended helices from ~6 to ~10 nm (highlighted by arrows in Fig. 1H). A large subpopulation of polyprolines, however, exhibited much shorter end-to-end distances contained in the respective first peak of the distribution. We speculate that these may arise in part because of pronounced bending and uncontrolled interactions with the surface, which differed from the solution-phase environment of previous studies.

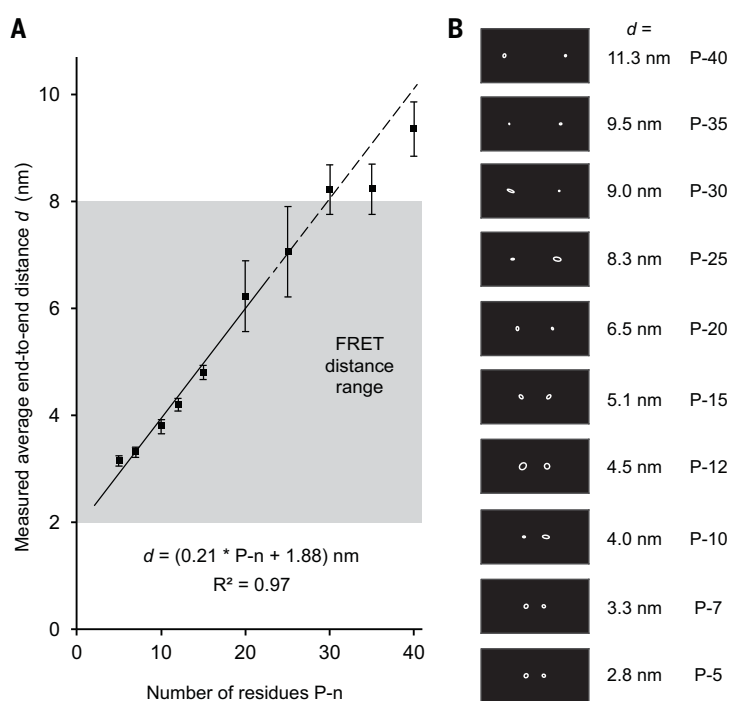
Up to 20 P, the average measured distances exhibited a close-to-linear scaling with the number of proline residues (Fig. 2A). Linear regression analysis in this range (P-5 to P-20) suggested an increment of $\Delta d \approx 0.21$ nm per proline residue. Although molecular dynam-

ics simulations would also explain moderate reductions of average end-to-end distance (33) for oligomers in this size range owing to chain bending, the observed increase of 2.1 Å, on average, per residue is in disagreement with PPII conformation of the helices in their entirety. For such all-trans bonding in the PPII conformation, which we expect to be generally favored under our experimental conditions, the helical pitch of 9.3 Å per turn and 3.0 residues per turn would result in an increase of 3.1 Å per residue. Instead, our data (Fig. 2A), falling short of the expected end-to-end distances of all-trans polyproline helices, may suggest heterogeneous compositions of cis and trans peptide-bond structural segments (37, 38), which, in combination, lead to the average linear scaling that was observed.

The constant offset (y intercept) of 1.9 ± 0.2 nm may be attributed in part to the fluorophores' displacement by the terminal glycine and lysine residues, which act as linkers, and to the fluorophores' physical size, which contributes additional distance to the "centers" of emission at both ends. In general, further contributions to distance variabilities may stem from motion or nonhorizontal attachments to the substrate and the two-dimensional (2D) projection measurement. Altogether, a horizontal alignment of example data shows that the entire "ladder" of intramolecular distances

Fig. 2. Intramolecular MINFLUX imaging of polyproline end-to-end distances.

(A) Measured average distances versus number of proline residues P- n . For P-5 to P-15, the averages were extracted as the positions of the peaks of the distributions in Fig. 1H. For P-20 and longer, an indication of the average more extended distances is given from the positions of the second, broader peaks. A linear fit over the P-5 to P-20 range is shown (solid line), suggesting an increase of, on average, 2.1 ± 0.2 Å per residue. The range of distances from ~2 to 8 nm has been traditionally addressed by (single-molecule) FRET methods (gray region). The dashed line indicates a continuation of the linear scaling from the fit. R^2 , goodness of fit. (B) Example data from Fig. 1, E to G, aligned by rotation to show the complete distance ladder (compare with Fig. 1C). The ellipses represent 3σ contours of localization uncertainty. Scale bar is 5 nm.



can be resolved and quantified (compare Figs. 1C and 2B) by MINFLUX.

Distance measurements on a small protein

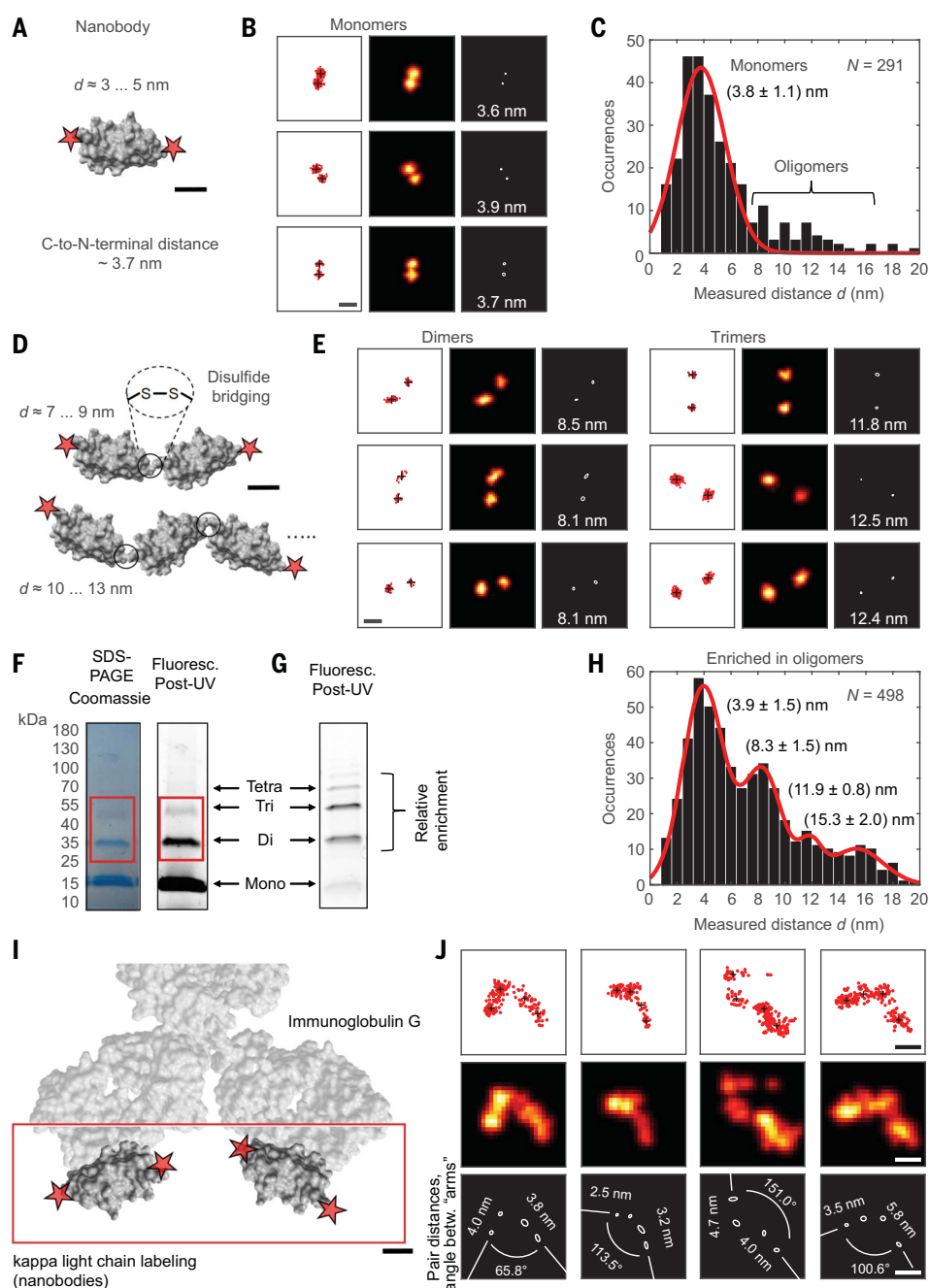
We next turned to examine C- and N-terminally labeled camelid nanobodies for end-to-end distance measurements. The core of this compact 16-kDa protein positions its C and N termini at a ~ 3.7 -nm distance (39) (Fig. 3A). The termini were labeled with a less hydrophobic photoactivatable dye (40), Abberior CAGE 635, by maleimide-coupling to the terminal cysteines. MINFLUX readily resolved this spacing, measuring (projected) distances predominantly in

the range of 2.5 to 5 nm (Fig. 3B). The distribution of distances (Fig. 3C) peaked at ~ 3.8 nm.

Interestingly, the distribution was accompanied by a tail of longer spacings, extending out to ~ 16 nm in rare instances. In particular, distances in the ranges of 7 to 9 nm and 10 to 13 nm (see examples in Fig. 3E) indicated the presence of nanobody dimers and trimers, respectively, whose end-to-end distances are expected to fall in this range. We hypothesized that dimers or trimers are formed by disulfide bridging (Fig. 3, D and E) of the free cysteines during the maleimide labeling protocol. A gradient-gel SDS-polyacrylamide gel electrophoresis (SDS-PAGE) analysis indeed revealed

dimers and trimers both in Coomassie stain and in the fluorescence observed after ultraviolet (UV) photoactivation (Fig. 3F and fig. S4). Owing to its high spatial resolution, MINFLUX had obviously identified the dimers and trimers directly by distance determinations despite their low abundance in the originally measured sample. Measurements of a mixture that was enriched in oligomers by size exclusion chromatography allowed us to assign subpopulations up to the size of tetramers at approximately multiples of the monomer end-to-end distance (Fig. 3H). Whereas the corresponding gel fluorescence (Fig. 3G) suggested less monomer, MINFLUX identified monomers as the most

Fig. 3. Intramacromolecular distance measurements: Sites on proteins and positioning of protein subunits. (A) Camelid nanobody (~ 16 kDa) with N and C termini cysteine-labeled with a photoactivatable dye. The dimensions of the prolate-shaped nanobody along the longer and shorter axes are ~ 4 nm by ~ 3 nm, and its N and C termini are 3.7 nm apart based on crystallographic data (39). (B) Corresponding MINFLUX example data. (C) Distribution of distances d obtained. The long tail of the distribution suggests the existence of nanobody dimers and trimers. The red curve is a Gaussian fit to estimate the peak position. (D) Distances attributed to dimers and trimers and (E) measurements corresponding to dimers (left) and trimers (right). (F) Coomassie stain and fluorescence of a gradient gel of the solution as imaged, with dimer and trimer bands highlighted by the red rectangles. (G) Gel fluorescence of a nanobody sample with a relative enrichment of dimers, trimers, and tetramers. (H) Distribution of measured distances for oligomer-enriched samples. A fit to a Gaussian model with four components (monomers, dimers, trimers, and tetramers) is shown (red curve). (I) IgG molecule, with the kappa light chains decorated by N- and C-terminal dye-labeled nanobodies, thus providing up to four positional fluorophore marks (indicated by stars) on the antibody molecule. (J) Examples of different orientations of the two IgG arms. Scale bars are 1 nm [(A), (D), and (I)] and 5 nm [(B), (E), and (J)].



abundant species, possibly as a result of different kinetics of surface adsorption among the different nanobody species. Note that the spacing of dimers, trimers, and tetramers (fig. S5) falls outside the FRET range, highlighting the ability of MINFLUX to measure distances >10 nm as well.

Subunit structural arrangements of a large protein

Next, we extended the demonstration of our method to more reporter fluorophore sites. To this end, we labeled immunoglobulin G (IgG) with C- and N-terminally dye-labeled (Abberior CAGE 635) nanobodies that have affinity for the IgG's kappa light chain. Up to four fluorophores were localized on the surface of the IgG. The fluorophores formed two pairs aligned with either of the two flexible "arms" of the IgG

(Fig. 3I). Owing to incomplete labeling and/or sampling (fig. S6A), not all fluorophore positions could always be extracted. Prolonged observation of individual dyes also indicated incomplete immobilization, as suggested in examples of relative displacements of one arm during acquisition (fig. S6B). However, those antibodies in which all four dyes were registered clearly displayed the orientation of the two IgG arms, with the pair distances of each assigned arm falling in the range of the (2D-projected) nanobody distances (Fig. 3J).

Measurements in cells

Next, we stably expressed a translational fusion of HaloTag to the N terminus of Lamin A/C in human osteosarcoma (U-2 OS) cells. Nuclear lamins are fibrous proteins that form

intermediate filaments, providing structural stability to the nucleus and influencing gene expression (41). The ~ 3.5 -nm-diameter filaments formed by lamins are substantially thinner than microtubular (24 nm), vimentin (10 nm), or actin (8 nm) filaments (42). Present models of the lamin structure (42, 43) suggest an assembly based on antiparallel pairings of dimers due to coiled-coil domain interactions (43). This arrangement explains the uniformly thick filament, along which globular Ig-like domains are positioned pairwise at the C termini of the individual lamins, on average every ~ 20 nm (Fig. 4A). The pairs of N termini in this arrangement are spaced at two unequal distances along the filament that add up to ~ 40 nm.

In our imaging experiments at the basal nuclear membrane, a dye-conjugated ligand bound

Fig. 4. Quantification of labeled protein distances in cells. MINFLUX imaging was used to examine the spatial distribution of HaloTag-Lamin A/C in the basal nuclear membrane of U-2 OS cells, where lamins form a filamentous meshwork. (A) Model of lamin filament molecular architecture (42, 43). An arrangement based on antiparallel pairings of dimers (43) is indicated. The N-terminally fused and fluorescently labeled (Abberior CAGE 635) pairs of HaloTags are positioned unevenly along the direction of the filament with a full period of ~ 40 nm, on either side of the C-terminal Ig-like domains that are known from electron microscopy to be spaced ~ 20 nm apart. (B) Examples of image regions. Arrows indicate sub-10-nm distances. Scale bars are 25 nm. (C) Examples of <10 -nm distance measurements. Scale bars are 5 nm. (D) Histogram of individually quantified distances <20 nm.

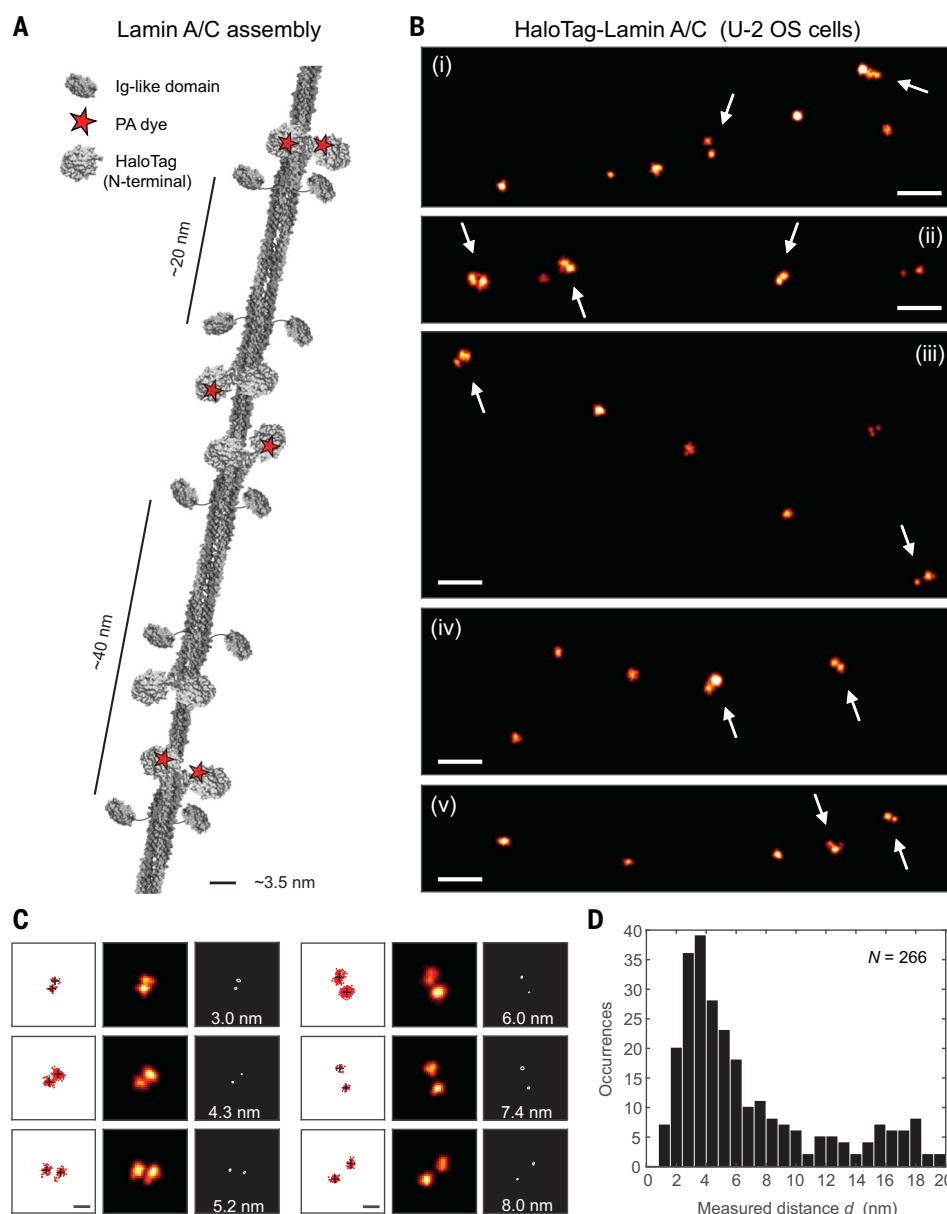
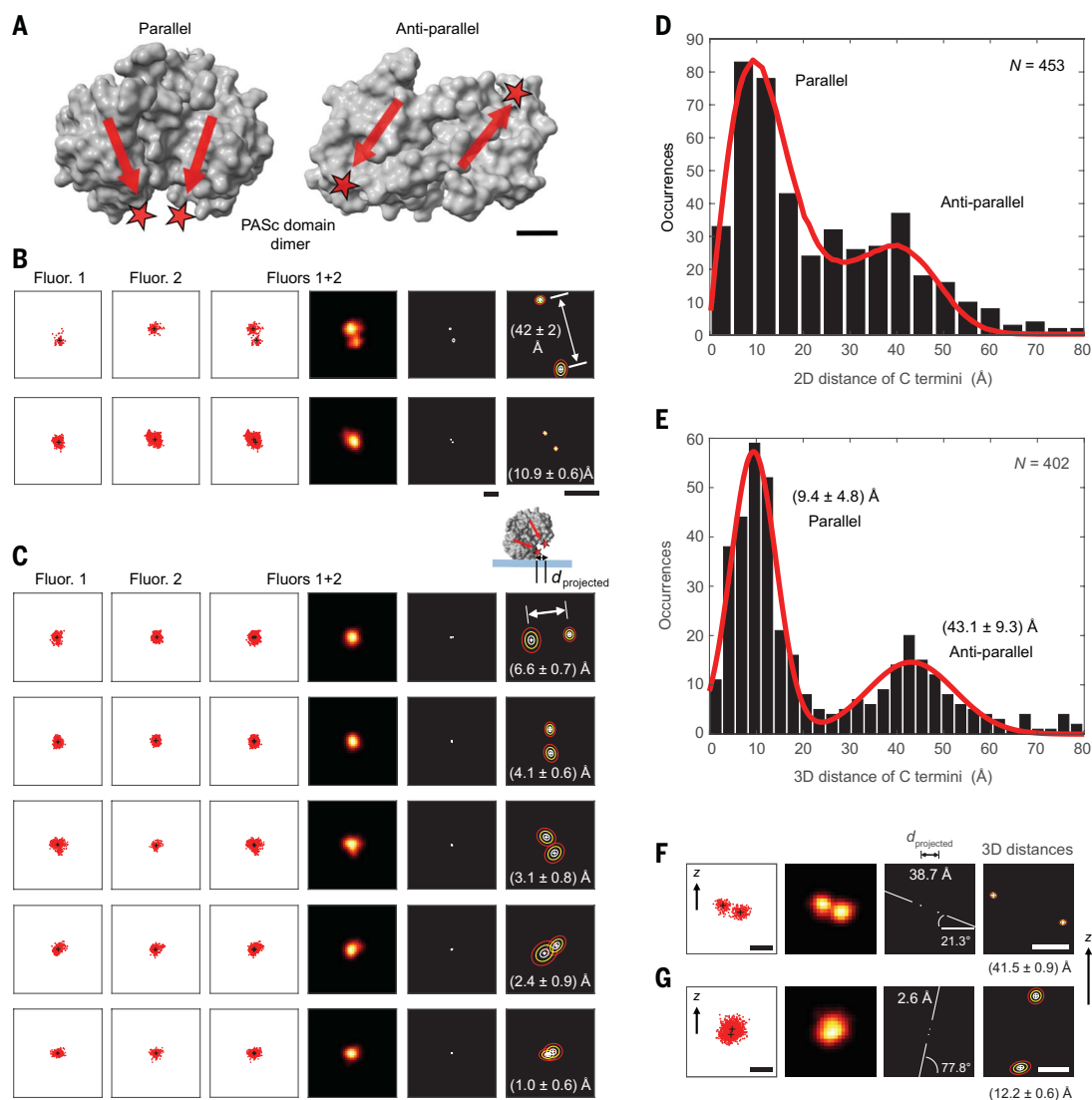


Fig. 5. Conformational measurements at and below FRET-range distances, and angstrom distance measurements: Protein domain dimer in parallel and antiparallel configuration.

(A) Crystallography data of the PASc domain of the bacterial citrate sensor histidine kinase (CitA) reveal that this dimer of protein domains exists in both antiparallel and parallel configurations. The separation of the C termini, labeled with two photoactivatable dyes (Abberior CAGE 635), differs between ~1 nm for the parallel dimeric arrangement and ~4 nm for the antiparallel dimer. (B) Examples of ~4- and ~1-nm distances. (C) Projected instances lead to distances <1 nm. The ellipses in the enlarged views on the right represent the 1σ (white), 2σ (yellow), and 3σ (red) contours of the position measurement uncertainty. (D) Distribution of all (2D-projected) C-terminal-to-C-terminal distances measured. Simulated projected distance distributions to capture the effects of the putatively random orientation of the dimers on the glass substrate can be found in fig. S10. Modeling with the assumption of isotropic orientations (red curve, see materials and methods) indicates a mixture of about half parallel, half antiparallel dimers. (E) Measured 3D distances clearly identify both populations. The red curve is a two-component Gaussian model fit. (F and G) Examples of orientations and distances in 3D. The data are shown in projection to a vertically (z) oriented plane through the two measured 3D coordinates. Distance measurements (1σ , 2σ , and 3σ contours indicated) and the respective angle with the horizontal are shown. The corresponding 2D-projected distance is also indicated. Scale bars are 1 nm (A), 5 nm and 2 nm (enlarged view) (B), 5 nm and 5 Å (enlarged view) (C), 5 nm and 2 nm (enlarged view) (F), and 5 nm and 5 Å (enlarged view) (G).



the HaloTag. Examples of 2D MINFLUX image regions (Fig. 4B) contained geometric arrangements of the labeled sites appearing to lie along a line, with pairs at small separation also seen. Incidentally, the shown regions merely span one diffraction zone (~300 nm across). Histograms of first nearest neighbor distances for the identified tag positions contain evidence for periodicities that can be accounted for by combinations of individual ~15-, ~25-, and ~40-nm separations (fig. S7). Numerous pairs of sites appear to correspond to the pairs of N termini (HaloTags) that are positioned directly adjacent. Because many of the first nearest neighbor distances also fell below 10 nm and could be reliably measured with high precision (Fig. 4, C and D; $N = 266$), these experiments demonstrate that

distances <10 nm can be directly quantified in cells.

Dimeric protein domains in parallel and antiparallel configuration: Down to angstrom distances

One of the exciting prospects of the newly gained resolution capability in the intramolecular range is the direct imaging of distance distributions from an ensemble of macromolecules. Biological structures do not adopt one rigid and non-varying arrangement. Molecules are flexible, and this flexibility should become visible in the many snapshots acquired. The resulting dataset is expected to contain the mean as the dominant structure, which is also observed by the averaging pursued in crystallography or cryo-electron microscopy. However, be-

cause the imaging of individual macromolecules maps out their conformational space, structural subpopulations become apparent by MINFLUX.

To demonstrate this capability, we investigated a protein domain dimer, the cytosolic PAS domain (PASc) of the bacterial citrate sensor histidine kinase (CitA) (44). Such a homodimeric system would be especially difficult to study by FRET because the approach typically relies on two different dyes. Crystallography data of PASc reveal that this dimer can assume both an antiparallel and parallel arrangement (45) (Fig. 5A). A pronounced quaternary structure rearrangement in the form of an antiparallel-to-parallel transition upon citrate binding is now thought to have a central role in transmitting and amplifying an

initially small structural change as part of the transmembrane signaling process (45).

The distance between the C termini, labeled with photoactivatable dyes (40), is expected to differ between ~1 nm (~10 Å) for the parallel dimeric arrangement and ~4 nm for the antiparallel dimer. In the imaging experiments, after sequential photoactivations (figs. S8 and S9), distance data were observed that ranged from the shortest distances of <1 nm, representing the parallel dimer at its full distance (or partially 2D-projected and thus reduced in length), to distances in the range of 4 nm, corresponding to the antiparallel arrangement (Fig. 5B). To appreciate the effects of the putatively random orientation of the dimers on the glass substrate, we simulated distributions of 2D-projected distances for species mixtures of various proportions (fig. S10). The data clearly contain a population of tilted dimers, for which the axis between the two fluorophores has a perpendicular component to the plane and for which distances between 0 and 1 nm were extracted with subangstrom measurement precision (Fig. 5C). The complete distribution (Fig. 5D; $N = 453$) indicates that about equal amounts of measured dimers were in the parallel and antiparallel states.

Equally angstrom-precise 3D position measurements (see materials and methods and fig. S11) provided additional information, allowing us to quantify the distribution of C-terminal separations as Euclidian 3D distances across the ensemble of sufficiently immobile dimers (Fig. 5E; $N = 402$). Uncompromised by planar projection, two distinct populations at 9.4 ± 4.8 and 43.1 ± 9.3 Å were identified, representing the parallel and antiparallel configurations in a nearly 2:1 mixture. MINFLUX thus quantified the relative abundance of the subpopulations with average C-terminal distances of ~1 and ~4 nm.

Individual examples of dimers measured to reside at different 3D orientations provide clear illustrations of the aforementioned 2D projection effects (Fig. 5, F and G): Species with mutual dye-dye separations of ~4 and ~1 nm are shortened in their x - y projected views to a reduced apparent distance, depending on orientation (fig. S12). Although the horizontally positioned molecules virtually agree in two and three dimensions, in the most extreme case, the projection shortens what is a ~12-Å species to ~2 Å in projection (Fig. 5G). The situation is readily interpreted as a parallel dimer standing almost orthonormal with the surface.

Conclusions

MINFLUX fluorophore localization down to ~0.1-nm precision enables accurate distance measurements down to the ~1-nm physical extent of the fluorophores (Fig. 5). For fluorophores positioned on macromolecules that lie at an angle and hence do not obstruct each

other along the distance to be measured, we quantified distances well below 1 nm. Resolving the end-to-end distance of small proteins and oligomers, these measurements provide optical access to the intra-macromolecular scale. As illustrated by distinguishing distances of 1 to 4 nm in parallel and antiparallel dimer configurations, MINFLUX also directly resolves subunits of proteins, as well as their relative orientation and conformation.

Our study further shows that intramolecular resolution can be directly obtained by observing just the two fluorophores at the end of the spatial interval in question. Unlike in camera-based localization, hundreds of copies of fresh fluorophores binding sequentially to the two sites over a long time are not needed.

Ensuring independent dye emissions (figs. S13 and S14), MINFLUX enables linear distance measurements not only over the FRET range (2 to 8 nm) but also below 2 to 3 nm, where FRET usually falters. For distances >8 nm, MINFLUX measurements are fully viable (Fig. 3, D and E). Indeed, because MINFLUX treats all distances equally, any distance from the diffraction scale (>200 nm) down to smallest values (<1 nm) is directly measurable with angstrom precision.

The present experiments certainly average over any rotational details in the combined localization information from the multiple individual position estimates, which are each obtained in ~1 ms (with the probing beam dwelling in one of the positions for only tens of microseconds at any given time in the MINFLUX implementation used). We anticipate that further developments of stable, bright dyes with near-unity photoactivation yields will further improve the applicability of our approach for studies of distance distributions within protein and other biomolecular systems, including in cells. Improved immobilization strategies to minimize the surface influence on proteins and the demonstrated 3D capability will be especially valuable in this regard. We also anticipate extensions to larger numbers of molecular sites.

With photoactivation as the on-off mechanism, we observe that no “10-nm resolution barrier” (18) was encountered, as for the STORM-type thiol-based blinking (46), nor did the approach require cryogenic temperatures (47, 48). Unlike sample expansion (49), which involves harsh chemical treatment, MINFLUX does not risk sample alterations at the sub-10-nm scale. The power of MINFLUX stems from the fact that it (i) can use established fluorescence labeling procedures and (ii) uses the fluorescence photon budget about 100 times more effectively than camera-based localization while also essentially avoiding (iii) molecular-orientation effects and (iv) FRET dipolar coupling.

Because it offers a high degree of spatial parallelization, a remaining advantage of camera-based FRET imaging is the large field of view,

which allows for the examination of many molecules simultaneously. However, ongoing efforts for parallelization of MINFLUX should translate the virtues of MINFLUX to larger fields of view and living cells. Finally, our work shows that fluorescence microscopy is undergoing a seminal transition from a method that merely maps out biomolecular spatial distributions in cells to one that directly reveals biomolecular function through precise determination of positions and distances with minimal invasiveness.

REFERENCES AND NOTES

1. T. Förster, *Ann. Phys.* **437**, 55–75 (1948).
2. T. Ha et al., *Proc. Natl. Acad. Sci. U.S.A.* **93**, 6264–6268 (1996).
3. G. J. Schütz, W. Traubinger, T. Schmidt, *Biophys. J.* **74**, 2223–2226 (1998).
4. X. Zhuang et al., *Science* **288**, 2048–2051 (2000).
5. R. Roy, S. Hohng, T. Ha, *Nat. Methods* **5**, 507–516 (2008).
6. L. Stryer, *Annu. Rev. Biochem.* **47**, 819–846 (1978).
7. W. R. Algar, N. Hildebrandt, S. S. Vogel, I. L. Medintz, *Nat. Methods* **16**, 815–829 (2019).
8. B. Hellenkamp et al., *Nat. Methods* **15**, 669–676 (2018).
9. G. Agam et al., *Nat. Methods* **20**, 523–535 (2023).
10. L. S. Churchman, Z. Ökten, R. S. Rock, J. F. Dawson, J. A. Spudich, *Proc. Natl. Acad. Sci. U.S.A.* **102**, 1419–1423 (2005).
11. A. Pertsinidis, Y. Zhang, S. Chu, *Nature* **466**, 647–651 (2010).
12. S. Niekamp et al., *Proc. Natl. Acad. Sci. U.S.A.* **116**, 4275–4284 (2019).
13. S. W. Hell, *Science* **316**, 1153–1158 (2007).
14. E. Betzig et al., *Science* **313**, 1642–1645 (2006).
15. M. J. Rust, M. Bates, X. Zhuang, *Nat. Methods* **3**, 793–795 (2006).
16. S. T. Hess, T. P. K. Girirajan, M. D. Mason, *Biophys. J.* **91**, 4258–4272 (2006).
17. T. Ha, P. Tinnefeld, *Annu. Rev. Phys. Chem.* **63**, 595–617 (2012).
18. D. A. Helmerich et al., *Nat. Methods* **19**, 986–994 (2022).
19. A. Sharonov, R. M. Hochstrasser, *Proc. Natl. Acad. Sci. U.S.A.* **103**, 18911–18916 (2006).
20. R. Jungmann et al., *Nano Lett.* **10**, 4756–4761 (2010).
21. M. Dai, R. Jungmann, P. Yin, *Nat. Nanotechnol.* **11**, 798–807 (2016).
22. S. C. M. Reinhardt et al., *Nature* **617**, 711–716 (2023).
23. S. M. Früh et al., *ACS Nano* **15**, 12161–12170 (2021).
24. J. Enderlein, E. Toprak, P. R. Selvin, *Opt. Express* **14**, 8111–8120 (2006).
25. S. Stallinga, B. Rieger, *Opt. Express* **18**, 24461–24476 (2010).
26. J. Engelhardt et al., *Nano Lett.* **11**, 209–213 (2011).
27. M. D. Lew, M. P. Backlund, W. E. Moerner, *Nano Lett.* **13**, 3967–3972 (2013).
28. F. Balzarotti et al., *Science* **355**, 606–612 (2017).
29. Y. Eilers, H. Ta, K. C. Gwosch, F. Balzarotti, S. W. Hell, *Proc. Natl. Acad. Sci. U.S.A.* **115**, 6117–6122 (2018).
30. P. M. Cowan, S. McGavin, *Nature* **176**, 501–503 (1955).
31. A. A. Adzhubei, M. J. E. Sternberg, A. A. Makarov, *J. Mol. Biol.* **425**, 2100–2132 (2013).
32. L. Stryer, R. P. Haugland, *Proc. Natl. Acad. Sci. U.S.A.* **58**, 719–726 (1967).
33. B. Schuler, E. A. Lipman, P. J. Steinbach, M. Kumke, W. A. Eaton, *Proc. Natl. Acad. Sci. U.S.A.* **102**, 2754–2759 (2005).
34. M. Weber et al., *Chem. Eur. J.* **27**, 451–458 (2021).
35. K. C. Gwosch et al., *Nat. Methods* **17**, 217–224 (2020).
36. R. Schmidt et al., *Nat. Commun.* **12**, 1478 (2021).
37. S. Dooze, H. Neuweller, H. Barsch, M. Sauer, *Proc. Natl. Acad. Sci. U.S.A.* **104**, 17400–17405 (2007).
38. R. B. Best et al., *Proc. Natl. Acad. Sci. U.S.A.* **104**, 18964–18969 (2007).
39. H. Götzke et al., *Nat. Commun.* **10**, 4403 (2019).
40. K. Kolmakov et al., *Photochem. Photobiol. Sci.* **11**, 522–532 (2012).
41. T. Dechat et al., *Genes Dev.* **22**, 832–853 (2008).
42. Y. Turgay et al., *Nature* **543**, 261–264 (2017).
43. J. Ahn et al., *Nat. Commun.* **10**, 3757 (2019).
44. M. Salvi et al., *Proc. Natl. Acad. Sci. U.S.A.* **114**, 3115–3120 (2017).

45. X. C. Zhang *et al.*, Mechanism of sensor kinase CitA transmembrane signaling. *bioRxiv* 2023.2002.2006.527302 [Preprint] (2023); <https://doi.org/10.1101/2023.02.06.527302>.
46. G. T. Dempsey *et al.*, *J. Am. Chem. Soc.* **131**, 18192–18193 (2009).
47. S. Weisenburger *et al.*, *Nat. Methods* **14**, 141–144 (2017).
48. P. D. Dahlberg *et al.*, *J. Am. Chem. Soc.* **140**, 12310–12313 (2018).
49. A. H. Shaib *et al.*, Expansion microscopy at one nanometer resolution. *bioRxiv* 2022.2008.2003.502284 [Preprint] (2022); <https://doi.org/10.1101/2022.08.03.502284>.
50. S. J. Sahl, Matlab scripts for: Direct optical measurement of intra-molecular distances with Ångström precision. Zenodo (2024); <https://doi.org/10.5281/zenodo.12744422>.

ACKNOWLEDGMENTS

We acknowledge excellent technical support at the Max Planck Institute (MPI) for Multidisciplinary Sciences (MPI-NAT) and the MPI for Medical Research (MPI-MR). The MINFLUX system (Abberior Instruments GmbH) was funded by the German Research Foundation (DFG; grant no. INST 186/1303-1 to S.J.). J. Bienert, J. Schimpfhauser, and J. Seikowski (all with the Facility for Synthetic Chemistry, MPI-NAT) coupled dyes to the proline polypeptides and synthesized the Halo-CAGE635 ligand. S. Fabritz (MPI-MR) performed mass spectrometry analysis. E. Rothermel (MPI-NAT) performed maleimide labeling of the nanobodies and cell staining. E. Rothermel, T. Koenen, and N. Jensen (MPI-NAT) helped in the creation of the Lamin A/C-Halo cell line. T. Koenen (MPI-NAT) cultured cells and helped with cell-line characterization. M. Sitte [NGS Integrative Genomics Core Unit, University Medical Center Göttingen (UMG)] evaluated sequencing data of the whole-exome sequencing analysis to validate the HaloTag-Lamin A/C cell line. G. Kostiuik helped with the size exclusion chromatography experiment. F. Opazo (UMG) advised on nanobody labeling.

K. Giller (MPI-NAT) produced the GtCitA PASC domain coupled with PA dye. R. Schmidt (Abberior Instruments GmbH) helped with early experiments on the optical setup that was later reported in (36). D. Jans (UMG and MPI-NAT) provided further guidance and support with MINFLUX imaging. A. Politi (Facility for Light Microscopy, MPI-NAT) provided support with additional testing. M. Leutenegger (MPI-NAT) simulated focal intensity distributions near the glass-liquid interface. T.A. Hensel (MPI-NAT) gave helpful input on change-point detection and correlation analysis methods. V.N. Belov (MPI-NAT) advised on chemical aspects and helped coordinate the dye coupling to the polypeptide rulers. **Funding:** This work was funded by the Max Planck Society (S.W.H.), German Research Foundation grant GR 1211/18-1 (C.G.), and the European Union's Horizon Europe Framework Programme (deuterON, grant agreement no. 101042046) (J.B.). This work was supported by the Deutsche Forschungsgemeinschaft (DFG, German Research Foundation) under Germany's Excellence Strategy - EXC 2067/1- 390729940. **Author contributions:** S.J.S. initiated and led the experimental exploration of emitter colocalization (direct position measurements) in the FRET distance regime and below to angstrom distances. S.J.S., J.M., and M.W. designed the imaging experiments. J.B. provided early input on the molecular model systems. J.M. identified the sustained fluorescence emission of the photoactivatable dyes. S.J.S., J.M., and K.I. performed the imaging experiments. S.J.S., J.M., and K.I. prepared samples for imaging. S.J.S. performed the data analysis, simulations, and interpretation, discussing with K.I., J.M., S.W.H., and the other co-authors. T.A.K. provided the photoactivatable silicon rhodamine fluorophore. M.W. biochemically confirmed the presence of oligomers, further developed the oligomerization reaction, and advised on photophysical properties of the photoactivatable dyes. M.W., C.B., and S.J. provided the HaloTag-Lamin A/C U-2 OS cell line based on a suggestion

of this target by M.W. S.B. and C.G. provided the GtCitA PASC domain dimers and structural comparisons by crystallography. S.W.H. conceived and developed the MINFLUX concept for ultraprecise, emission-photon-efficient localization and provided critical feedback during the project. S.J.S. and S.W.H. wrote the manuscript, and all co-authors discussed the results and approved the final version of the manuscript. **Competing interests:** S.W.H. holds shares of Abberior Instruments and has revenues through MINFLUX patents held by the Max Planck Society. J.M. is an employee of Abberior Instruments America LLC. All other authors declare that they have no competing interests. **Data and materials availability:** The data that support the findings of this study are provided in the main text or the supplementary materials. The Matlab code used for the localization data segmentation, distance evaluations, and data display has been deposited at Zenodo (50). **License information:** Copyright © 2024 the authors, some rights reserved; exclusive licensee American Association for the Advancement of Science. No claim to original US government works. <https://www.science.org/about/science-licenses-journal-article-reuse>

SUPPLEMENTARY MATERIALS

[science.org/doi/10.1126/science.adj7368](https://doi.org/10.1126/science.adj7368)

Materials and Methods

Supplementary Text

Figs. S1 to S14

Tables S1 to S3

References (51–54)

MDAR Reproducibility Checklist

Submitted 13 July 2023; accepted 3 September 2024
10.1126/science.adj7368